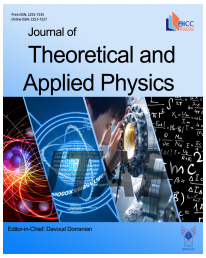

Volume 18, Issue 5, 182466 (1-9)

Journal of Theoretical and Applied Physics (JTAP)

https://dx.doi.org/10.57647/j.jtap.2024.1805.66

Investigation of the effect of bismuth-oxide on the X-ray and neutron shielding efficacy of the new ceramic system Bi_2O_3–BaO–Fe_2O_3–SrO–B_2O_3

Bonginkosi V. Kheswa, Siyabonga N. T. Majola

Department of Physics, University of Johannesburg, 55 Beit Street, Doornfontein, South Africa.

*Corresponding author: vincentk@uj.ac.za

Original Research

Received:
8 June 2024
Revised:
21 September 2024
Accepted:
27 September 2024
Published online:
30 October 2024

Abstract:

X-rays and neutrons, vital in numerous industries, necessitate effective shielding to mitigate health risks. Traditional shielding materials like lead and concrete pose issues such as toxicity and structural limitations. This has driven global research towards exploring non-toxic heavy metal oxide glass materials for enhanced radiation protection. This study examined the impact of Bi_2O_3 on the radiation shielding efficiency of a glass composition $(x)Bi_2O_3 - (20 - x)BaO - 60Fe_2O_3 - 0.3SrO - 19.7B_2O_3$, with x values of 0, 5, 10, 15, and 20 mol%, over the 15 to 300 keV X-ray range. The Linear Attenuation Coefficient (LAC) of this glass series increased by 12%, 1.7%, and 13% in the energy ranges of 15 – 30 keV, 40 – 80 keV, and 100 – 300 keV, respectively, per 1 mol% Bi_2O_3 increase. The Half Value Layer (HVT), Tenth Value Layer (TVT), and Mean Free Path (MFP) decrease by 4% per mol% of Bi_2O_3 at energies less than 40 keV and above 100 keV, while decreasing at a rate of 1% in the 40 – 100 keV region. Sample S1, without Bi_2O_3, exhibited the lowest shielding efficiency, while sample S5, with the highest Bi_2O_3 content, demonstrated the highest shielding efficiency. Increasing Bi_2O_3 concentration notably improves X-ray shielding efficacy, especially below 40 keV and above 100 keV.

Keywords: Shielding; Lead-free; X-ray; Glass; Attenuation

1. Introduction

The usage of ionizing radiation in various industries is inevitable due to the advancements in modern technology. Two types of such radiation are X-rays and neutrons, which serve in multiple applications such as inspection of printed circuit boards, computed tomography scans, Radiotherapy, dental imaging, and many other radiographic testing. However, without proper shielding, X-rays and neutrons pose significant health hazards to personnel in these industries. There exists a plethora of materials suitable for shielding against X-rays and neutrons. Traditionally, lead plates and concrete have been employed for shielding. However, these materials present various drawbacks, including lead toxicity and the cumbersome nature of moving and maintaining both lead and concrete [1–3]. Moreover, prolonged exposure to nuclear radiation can induce heating in concrete, leading to structural integrity issues such as cracking and potential radiation leakage [2, 4, 5]. Additionally, the lack of light transparency in lead and concrete poses challenges for real-time observation, hindering the timely detection of irregularities where visual monitoring is crucial [2]. Consequently, there is considerable global research interest in identifying optimal heavy metal oxide glass materials, which are lead-free, for ionizing electromagnetic radiation shielding [6–29]. For instance, recent studies have investigated various glass compositions, revealing promising findings. Studies on bismuth-borate glass doped with rare-earth ions indicated enhanced X-ray shielding efficacy, with samarium-doped glass outperforming neodymium and cerium counterparts [16]. Computational investigations into $Bi_2O_3 - B_2O_3 - TeO_2 - TiO_2$ glass for X-ray shielding within the 30 to 80 keV energy range highlighted its potential for protective mask fabrication during oral cavity irradiation [17]. Similarly, research on $Li_2O - B_2O_3 - MgO - Er_2O_3$ glass, doped with Sm_2O_3, demonstrated im-

proved photon shielding capabilities with increasing Sm_2O_3 content [18]. Investigations into La_2O_3 – CaO – B_2O_3 – SiO_3 glass revealed enhanced X-ray shielding efficiency with higher La_2O_3 content [19]. Moreover, recent studies explored the photon shielding properties of borate glass compositions, revealing enhancements with the inclusion of various additives, namely Cr_2O_3, TeO_2, Gd_2O_3, WO_3, TeO_2/MoO_3, and CeO_2 [20–26]. In the same vein, Ref. [27] investigated bulk metallic glass samples and showed that $Ti_{41.9}Zr_{36.3}V_{12.1}Cu_{6.3}Be_{3.4}$ which has the lowest Ti and highest Zr contents has the superior radiation shielding capability among the studied samples. The study of Ref. [28] explored the impact of Ag content on neutron shielding properties of glass samples and revealed enhancements with increased Ag concentration. Furthermore, computational analyses of $Li_2B_4O_7$ – Bi_2O_3 – ZrO_4 – $CaWO_4$ highlighted improved neutron shielding efficiency with higher Bi_2O_3 concentration [29]. Moreover, Ref. [30] investigated the impact of Dy concentration on the neutron shielding efficacy of $15Li_2O$ – 25BaO – $(40–x)B_2O_3$ – $20P_2O_5$ – $(x)Dy_2O_3$ ($x = 0$, 0.2, 0.4, 0.6, 0.8, and 1.0 mol%), and showed that the sample with no Dy has the highest fast neutron removal cross sections (FNRCS). In the work of Ref. [31], the fast and slow neutron removal cross sections of five SiO_2 – Pb_3O_4 – $(5-x)$ZnO – $(x)WO_3$ glass samples were studied. The results revealed that both slow and fast neutron removal cross sections improve with the increase in the concentration of WO_3. Similarly, the study of Ref. [32] investigated neutron shielding characteristics of Y_2O_3 reinforced B_2O_3 – SiO_2 – BaO – Na_2O glass configuration, and showed that FNRCS increase with the enhancement in Y_2O_3 concentration.

In this study, we delve into a comprehensive examination of the X-ray and fast neutron shielding capabilities of the five novel glass compositions, comprising $(x)Bi_2O_3$ – $(20-x)$BaO – $60B_2O_3$ – $0.3Fe_2O_3$ – 19.7SrO, where $x = 0$, 5, 10, 15, 20 mol%. These were recently synthesized by Ref. [33], but their neutron shielding characteristics and X-ray shielding properties (in the energy region below 280 keV) remain unexplored. Specifically, computational assessments were carried out to evaluate key parameters including the mass attenuation coefficient (MAC), linear attenuation coefficient (LAC), half-value layer (HVL), tenth-value layer (TVL), mean-free path (MFP), effective electron density (Neff), and fast neutron removal cross sections (FNRCS). Thus, this work quantitively and systematically reveals the effect of Bi_2O_3 on the $(x)Bi_2O_3$ – $(20-x)$BaO – $60B_2O_3$ – $0.3Fe_2O_3$ – 19.7SrO glass configuration. Bismuth is preferred in heavy metal oxide glasses for radiation shielding applications, just like in perovskite solar cells, because it is a non-toxic heavy element, unlike Pb which is toxic.

2. Computational tools and theoretical framework

Analysis of the X-ray and fast neutron shielding properties of our five glass samples was conducted using Phy-X/PSD software. Phy-X/PSD operates on a remote server equipped with an Intel(R) Core(TM) i7-2600 CPU @ 3.40 GHz processor and 1 GB of installed memory, running on the Ubuntu 14.04.3 LTS operating system [34, 35]. Across the energy range of 15 keV to 300 keV, Phy-X/PSD was employed to compute MAC, LAC, HVL, TVL, MFP, and Neff of the five glass samples $20BaO – 60B_2O_3 – 0.3Fe_2O_3 – 19.7SrO$, $5Bi_2O_3$– 15BaO – $60B_2O_3$ – $0.3Fe_2O_3$ – 19.7SrO, $10Bi_2O_3$– 10BaO – $60B_2O_3$ – $0.3Fe_2O_3$ – 19.7SrO, $15Bi_2O_3$– 5BaO – $60B_2O_3$ – $0.3Fe_2O_3$ – 19.7SrO, and $20Bi_2O_3 – 60B_2O_3 – 0.3Fe_2O_3$ – 19.7SrO, which are denoted by S1, S2, S3, S4, and S5 in the rest of this document. The FNRCS of the samples were also computed with Phy-X/PSD. The densities of these glass systems, which are some of the input data used in the calculations, are shown in Figure 1. The theoretical framework of these radiation shielding calculations is provided below. The linear attenuation coefficient (μ) serves as a metric for assessing the probability of photon interaction with radiation shielding material, encompassing contributions from the photoelectric effect, Compton scattering, and pair production. This coefficient's variation with photon energy (E) and absorber atomic number (Z) mirrors the dependencies of these processes on E and Z. The linear attenuation coefficient (LAC) is governed by the Beer-Lambert law, linking it to both photon intensity and absorber thickness, x, as follows [35]

$$I(x) = I_0 e^{(-\mu x)} \tag{1}$$

where I_0 and $I(x)$ represent the photon intensities before and after traversing an absorber with thickness x, respectively. The effectiveness of attenuating X-rays is directly linked to the value of μ. A higher μ value implies enhanced material capability in attenuating radiation.

Similarly, the mass attenuation coefficient (MAC) provides a measure of the probability of attenuating X-rays within an absorber material. However, in contrast to the linear attenuation coefficient, it remains independent of material density. Instead, the mass attenuation coefficient is solely determined by the photon energy and the absorber's intrinsic structure. It is calculated according to [35]

$$\mathrm{MAC} = \sum w_i \left(\frac{\mu}{\rho}\right)_i \tag{2}$$

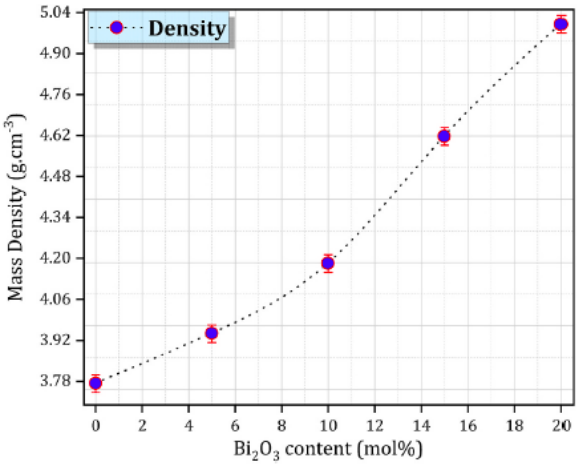

Figure 1. Density of the glass samples S1, S2, S3, S4, and S5 [33].

where w_i represents the weight of the i^{th} constituent element in the absorber.

The half-value thickness (HVT) and tenth-value thickness (TVT) stand as crucial parameters in explicating the shielding efficacy against X-ray radiation. Analogous to the temporal concept of half-life in nuclear decay phenomena, the HVT denotes the material thickness requisite to halve the initial photon intensity. Likewise, the TVT signifies the absorber thickness needed to diminish photon intensity by a factor of ten. A reduction in both HVT and TVT values indicates enhanced efficiency in radiation attenuation. These are computed from the linear attenuation coefficient as follows [35]

$$\mathrm{HVT} = \frac{0.693}{\mu} \tag{3}$$

and

$$\mathrm{TVT} = 3.32\,\mathrm{HVT} \tag{4}$$

Moreover, the mean free path (MFP) represents the mean distance traversed by a photon within an absorber before encountering either photoelectric effect, Compton scattering, or pair production. Materials exhibiting lower MFP values are regarded as more proficient in shielding X-rays compared to those with higher MFP values. It is given by [35]

$$\mathrm{MFP} = 1.44\,\mathrm{HVT} \tag{5}$$

The effective atomic number (Z_{eff}) is derived from the linear attenuation coefficient and the density of an absorber, as specified in the expression below [35].

$$Z_{eff} = \frac{\sum_j f_j A_j \left(\frac{\mu}{\rho}\right)_j}{\sum_j \frac{f_j A_j}{Z_j} \left(\frac{\mu}{\rho}\right)_j} \tag{6}$$

where f_j, A_j, and Z_j denote the mole fraction, atomic weight, and atomic number of each constituent element within the sample, respectively. Higher values of Z_{eff} correspond to heightened radiation shielding efficacy exhibited by the material.

The effective electron density (N_{eff}) of each glass sample is computed from its MAC using the equation [35, 36]

$$N_{eff} = \frac{\mathrm{MAC}}{\sigma_e} \tag{7}$$

where σ_e is the total electronic cross-section which is obtained

$$\sigma_e = \frac{\frac{\mathrm{MAC}}{N_A \sum_i (w_i/A_i)}}{Z_{eff}} \tag{8}$$

The variables A_i and w_i are atomic weight and weight fraction of the i^{th} elements in the sample, respectively, while N_A is the Avogadro´s number.

Furthermore, in neutron beam applications, the effectiveness of each glass sample in attenuating neutrons can be assessed using the fast neutron removal cross sections (FNRCS), $\sum_R$. This parameter measures the likelihood that neutrons will be attenuated within a material. The higher the $\sum_R$ value, the better the material is in reducing neutron intensity as the neutrons pass through it. It is computed using [34]

$$\sum_R = \sum_i (W_i \sum_{Ri}) \tag{9}$$

where W_i and $\sum_{Ri}$ are, respectively, partial density and fast neutron removal cross sections (in cm^2/g) of the i^{th} constituent element of the absorber material. The partial density of each element is obtained from the weight fraction, S_i,of the element and density, ρ, of the absorber according to

$$W_i = S_i \rho \tag{10}$$

3. Results and discussions

In this section, we discuss our new results on the dependence of the radiation shielding efficacy, of the $(x)Bi_2O_3 - (20-x)BaO - 60B_2O_3 - 0.3Fe_2O_3 - 19.7SrO$ glass family, on the Bi_2O_3 concentration. Table 1 shows the mass

Table 1. The mass attenuation coefficient of S1, S2, S3, S4 and S5 computed with Phy-X/PSD.

E (keV)	S1	S2	S3	S4	S5
15	23.487 ± 0.939	38.386 ± 1.535	49.546 ± 1.982	58.218 ± 2.329	65.151 ± 2.606
20	20.917 ± 0.837	33.246 ± 1.330	42.481 ± 1.699	49.657 ± 1.986	55.394 ± 2.216
30	7.103 ± 0.284	11.510 ± 0.460	14.811 ± 0.592	17.376 ± 0.695	19.427 ± 0.777
40	9.182 ± 0.367	9.188 ± 0.368	9.192 ± 0.368	9.196 ± 0.368	9.198 ± 0.368
50	5.150 ± 0.206	5.152 ± 0.206	5.154 ± 0.206	5.155 ± 0.206	5.156 ± 0.206
60	3.197 ± 0.128	3.209 ± 0.128	3.217 ± 0.129	3.224 ± 0.129	3.229 ± 0.129
80	1.526 ± 0.061	1.544 ± 0.062	1.557 ± 0.062	1.567 ± 0.063	1.575 ± 0.063
100	0.880 ± 0.035	1.718 ± 0.069	2.346 ± 0.094	2.834 ± 0.113	3.224 ± 0.129
150	0.362 ± 0.014	0.662 ± 0.026	0.887 ± 0.035	1.062 ± 0.042	1.201 ± 0.048
200	0.220 ± 0.009	0.363 ± 0.015	0.470 ± 0.019	0.553 ± 0.022	0.620 ± 0.025
300	0.133 ± 0.005	0.184 ± 0.007	0.221 ± 0.009	0.251 ± 0.010	0.274 ± 0.011

attenuation coefficient (MAC) of S1, S2, S3, S4, and S5 as a function of photon energy in the energy range of $15-300$ keV. We observe that the MAC increases with an increase in the Bi_2O_3 in the energy ranges of 15 to 30 keV, and 100 to 300 keV, with S1 and S5 remaining the lowest and highest, respectively. On the other hand, the MAC remains relatively constant in the 40 to 80 keV energy region. At these energies, S1, which does not contain Bi_2O_3, is comparable to the S2, S3, S4, and S5. This is because of the sharp increase in the MAC of S1 resulting from the K-edge electrons, which have enhanced contribution to the photoelectric effect component of the MAC. A similar sharp increase in the S2, S3, S4, and S5 is observed at 100 keV. This is attributed to the K-absorption edge resulting from the addition of Bi_2O_3. The enhancement in the MAC due to K-edge electrons has been reported in other studies in the literature [37]. Furthermore, Table 1 shows that on average, the MAC is the fast-decreasing function of energy. This is because the photoelectric cross-section, which is dominant in this energy region, is inversely proportional to $E3.5$, where E is the photon energy. In particular, the MAC of S1, which is the lowest in the 15 to 30 keV and 100 to 30 keV regions, ranges from 23.487 to 0.133 cm^2/g, S5 which is the highest in these energy regions ranges from 65.151 to 0.274 cm^2/g.

Figure 2 shows the linear attenuation coefficient (LAC) of S1, S2, S3, S4, and S5 as a function of X-ray energy. The LAC shows trends that are similar to those of the MAC, and this is consistent with Equation (2) which relates the MAC to the LAC. However, unlike the MAC, the linear attenuation coefficient increases with an increase in the Bi_2O_3/BaO ratio, even in the 40 to 100 keV region. A similar trend has been reported in other studies [38]. The glass sample S1 is the lowest in the whole 15 to 300 keV energy range, while S5 is the highest at all X-ray energies. The LAC of S1 ranges between 88.780 and 0.504 cm^{-1},

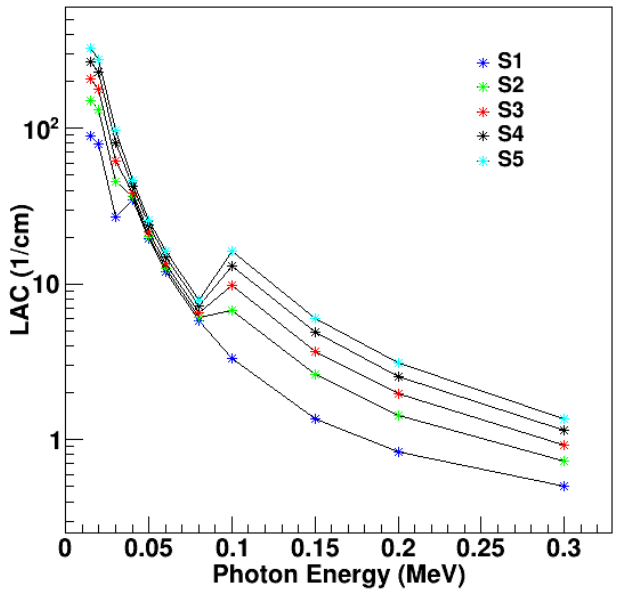

Figure 2. Linear attenuation coefficient as a function of photon energy.

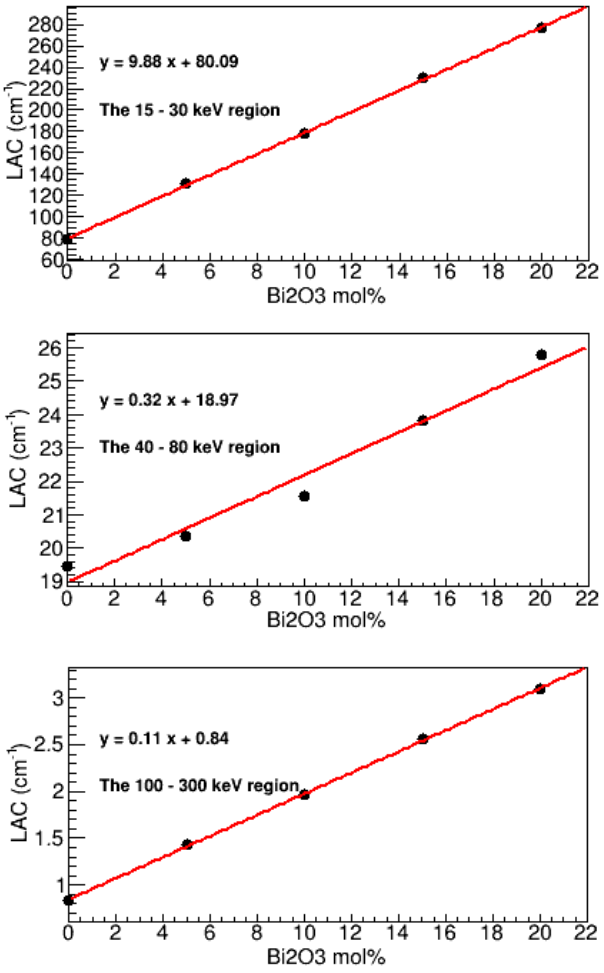

Figure 3. Variation of the LAC with the mol% of Bi_2O_3 at three energy regions.

while it ranges between 325.755 and 1.371 cm^{-1} for S5. The enhancement in the linear attenuation coefficient with the increase in the Bi_2O_3/BaO ratio results from the fact that the photo-absorption cross section is proportional to Z^5, where Z is the atomic number of an absorber material, and the Z of Bi is much higher than that of Ba.

We also conducted a thorough quantitative examination of the dependence of the linear attenuation coefficient, of our five glass samples, on the Bi_2O_3 concentration in the three X-ray energy regions, namely 15 to 30 keV, 40 to 80 keV, and 100 to 300 keV. In particular, we explored the variation of the LAC with Bi_2O_3 and extracted the percentage rate at which the LAC changes with the mol% of Bi_2O_3. This is depicted in Figure 3, which shows this linear relationship at the photon energies of 20 keV, 50 keV, and 200 keV, which are, respectively, within $15-30$ keV, $40-80$ keV, and $100-300$ keV energy ranges. This linear increase of LAC with Bi_2O_3 concentrations is consistent with the literature [10]. Nevertheless, at 20 keV the LAC increases by $\delta = (9.88/80.09) \times 100 = 12\%$ per 1% mol of Bi_2O_3, while at 50 and 200 keV, it increases by $\delta = 1.7\%$ and $\delta = 13\%$ per 1% mol of Bi_2O_3, respectively. Figure 2 suggests that the δ values remain approximately constant in their entire respective energy regions. Thus, the LAC in the

15 to 30 keV X-ray energy range increases 7 times faster than it does in the 40 keV to 80 keV region, for every 1% mol of Bi_2O that is added to the system, while for X-ray energies above 100 keV, it creases 8 times faster than it does at energies between 40 keV and 80 keV.

Furthermore, Figure 4 shows the mean free path (MFP) of S1, S2, S3, S4, and S5 in the 15 to 300 keV X-ray energy region. The new MFP of S1 increases fast with the increase in photon energy, as the energy approaches 30 keV, after which it sharply decreases at 40 keV and continues to increase fast as a function of energy. On the other hand, S2, S3, S4, and S5 rise fast with energy up to 80 keV, and suddenly decrease at 100 keV and continue increasing as the energy approaches 300 keV. The sudden decrease in the MFP at 40 keV and 100 keV is due to the K-edge electrons which suddenly increase the photo-absorption cross-sections at these energies, and thus, drastically reduce the mean-free path. It is also evident that S1 which has the lowest Bi_2O_3 concentration has the highest MFP in the whole energy region, while S5 which has the highest Bi_2O_3 content has the lowest MFP. This means that the mean free path decreases with an increase in the Bi_2O_3/BaO ratio. This trend is similar to the recent observations that have been reported in the literature [39]. In particular, it ranges from 0.011 to 1.985 cm for S1 and 0.003 to 0.729 cm for S5.

In the same vein, Figures 5 and 6 depict the half-value thickness (HVT) and tenth-value thickness (TVT) of our five glass samples as a function of photon energy. The HVT and TVT reveal a trend similar to that of the MFP. Thus, further confirming that the radiation shielding ability of the $(x)Bi_2O_3 - (20-x)BaO - 60B_2O_3 - 0.3Fe_2O_3 - 19.7SrO$ glass network improves with an increase in the Bi_2O_3 concentration, and reduces with an increase in the X-ray energy. The HVT and TVT of sample S1 remain the highest in the entire 15 to 300 keV photon energy range, while S5 is the lowest. The sudden reduction in HVT and TVT at 40 keV and 100 keV due to the K-absorption edges is also revealed.

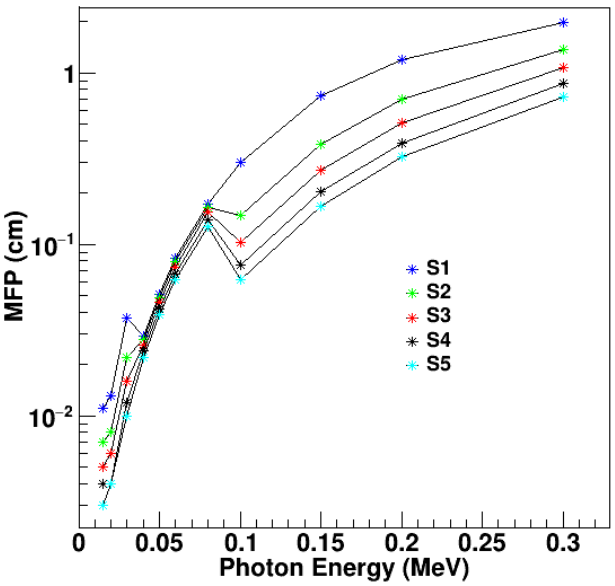

Figure 4. Mean free path as a function of photon energy.

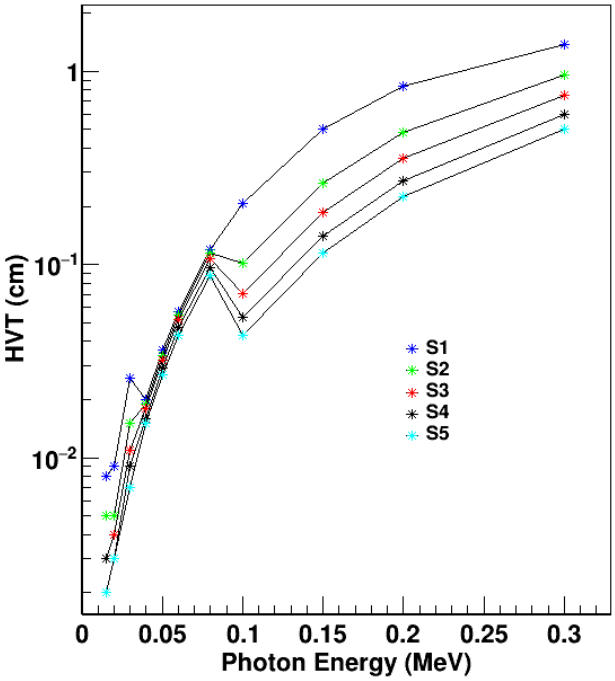

Figure 5. Half-value thickness as a function of photon energy.

Similar reductions in these quantities have been recently reported in other studies [39]. Quantitatively, the HVT and TVT of S1, respectively, range from 0.008 to 1.376 cm and 0.026 to 4.571 cm, while for S5 they are in the range of 0.002 to 0.506 cm and 0.007 to 1.679 cm, respectively.

We also conducted a thorough examination of the rates at which the MFP, HVT, and TVT change with the increase in the Bi_2O_3 concentration, at energies of 15 to 30 keV, 40 to 80 keV, and 100 to 300 keV, using the same approach that was employed for the LAC and depicted in Figure 4. The results showed that MFP, HVT, and TVT, decrease by 4% at X-ray energies of $15-30$ keV, and $100-300$ keV, per 1% mol of Bi_2O_3 that is added to the system, while they decrease by 1% in the 40 to 80 keV energy region.

Furthermore, Figure 7 shows the effective electron density (N_{eff}) of glasses S1, S2, S3, S4, and S5 in the photon energy region of 15 to 300 keV. The N_{eff}, on average, decreases fast with an increase in the X-ray energy. The sample S1, which has the lowest Bi_2O_3 concentration, has the smallest effective electron density at energies below 40 keV, while S2, S3, S4, and S5 are higher and comparable. In the 40 to 80 keV energy region, all samples have practically the same N_{eff}. This is because the K-edge electrons in S1 greatly enhance the magnitude of N_{eff} at these energies. At X-ray energies greater than 100 keV, S1 remains the lowest, and S2, S3, S4, and S5 are significantly higher due to the K-edge electrons of Bi, and the N_{eff} clearly improves with an increase in Bi_2O_3 content. The trends revealed by N_{eff} are consistent with our observations in MAC, LAC, MFP, HVT, and TVT, which show significant improvements at energies below 40 keV and above 100 keV, with an increase in Bi_2O_3, but little improvement in the 40 to 80 keV energy range.

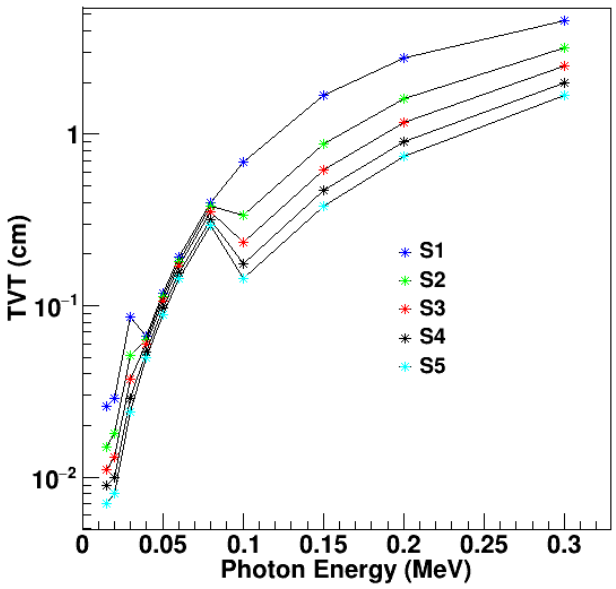

Figure 6. Tenth-value thickness as a function of photon energy.

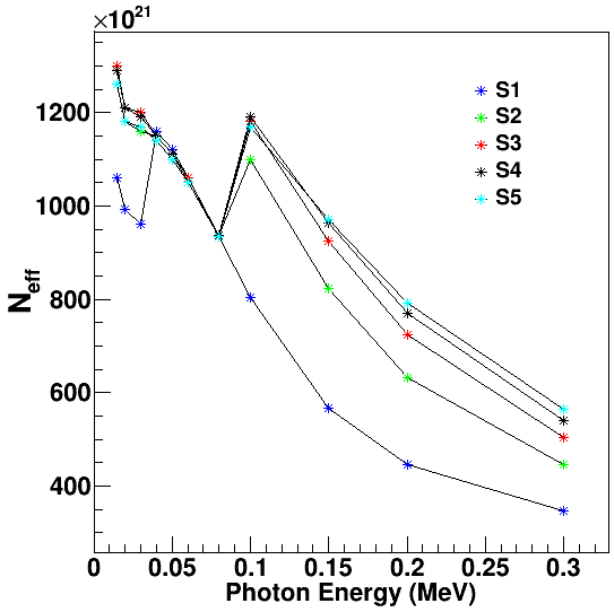

Figure 7. Effective electron density as a function of photon energy.

The fast neutron removal cross sections of S1, S2, S3, S4, and S5 are depicted in Figure 8. We observe that S1 > S2 > S3, and S3 < S4 < S5. This means that FNRCS decrease as the Bi_2O_3 concentration increases from 0 to 10% mol, and it increases again as Bi_2O_3 concentration increases from 10 to 20% mol. This trend can be attributed to the dependence of FNRCS on the weight fractions of the constituent elements, as described by Equation (9). In the range from 0 to 10% mol Bi_2O_3, the weight fractions of other elements, including boron—which has the highest $\sum_{Ri}$ (see Table 2)—decrease. This reduction leads to lower FNRCS for samples S2 and S3. This also means that although boron is known for being efficient in neutron absorption, its contribution to our glass system deteriorates with the increase in Bi_2O_3 content. In contrast, for samples S4 and S5, the weight fraction of Bi increases significantly (to 45% in S4 and 54% in S5, see Table 2) as the Bi_2O_3 concentration approaches 20% mol. Thus, Bi starts to significantly affect the FNRCS, leading to the observed increase in samples S4 and S5. Sample S5 which has FNRCS of 0.115 cm^{-1} is the only one slightly higher than S1 which has FNRCS of 0.114 cm^{-1}.

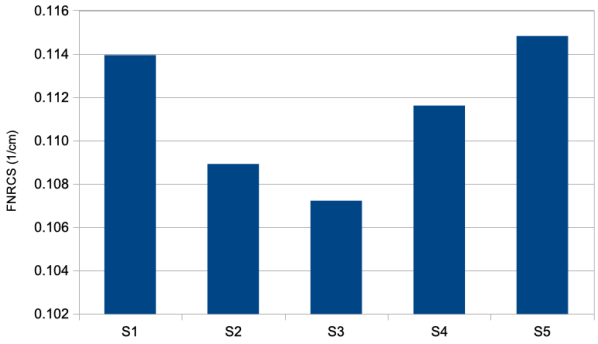

Figure 8. Fast neutron removal cross sections of S1, S2, S3, S4, and S5.

4. Conclusion

The study evaluated the impact of varying Bi_2O_3 concentration on the radiation shielding effectiveness of the glass composition $(x)Bi_2O_3 - (20-x)BaO - 60Fe_2O_3 - 0.3SrO - 19.7B_2O_3$ with x values of 0, 5, 10, 15, and 20% mol,

Table 2. Weight fractions and $\sum_{Ri}$ of constituent elements of S1, S2, S3, S4, and S5.

	$\sum_{Ri}$ (cm^2/g)	S_i in S1	S_i in S2	S_i in S3	S_i in S4	S_i in S5
Ba	0.0129	0.2943	0.1890	0.1102	0.0490	0.0000
O	0.0405	0.3782	0.3386	0.3090	0.2859	0.2675
B	0.0575	0.1390	0.1191	0.1041	0.0925	0.0832
Fe	0.0214	0.0036	0.0031	0.0027	0.0024	0.0021
Sr	0.016	0.1849	0.1584	0.1385	0.1231	0.1108
Bi	0.0103	0	0.1918	0.3355	0.4471	0.5363

across 15 to 300 keV X-ray energies. Findings revealed that the LAC of this glass series increased by 12%, 1.7%, and 13% in the energy ranges of 15 to 30 keV, 40 to 80 keV, and 100 to 300 keV, respectively, per 1% mol increase in Bi_2O_3. The HVT, TVT, and MFP decrease by 4% per mol% of Bi_2O_3 at energies below 40 keV and above 100 keV, whereas they decrease by 1% per mol% within the 40 to 80 keV range. Sample S1 (no Bi_2O_3) had the lowest MAC, LAC, and highest HVT, TVT, and MFP, with values from $23.487 - 0.133$ cm^2/g, $88.780 - 0.504$ cm^{-1}, $0.008 - 1.376$ cm, $0.026 - 4.571$ cm, and $0.011 - 1.985$ cm. Sample S5 (highest Bi_2O_3) showed the highest MAC, LAC, and lowest HVT, TVT, and MFP, ranging from $65.151 - 0.274$ cm^2/g, $325.755 - 1.371$ cm^{-1}, $0.002 - 0.506$ cm, and $0.007 - 1.679$ cm, $0.003 - 0.729$ cm. Thus, increasing Bi_2O_3 boosts X-ray shielding efficacy, especially below 40 keV and above 100 keV, with negligible effects between 40 and 80 keV. This conclusion is further supported by the trends revealed by N_{eff} of the five glass samples. The results also revealed that increasing Bi_2O_3 concentrations from 0 to 15% mol led to a decrease in the fast neutron removal cross section (FNRCS). However, at 20% mol, the FNRCS improved, with S5 showing the highest value 0.115 cm^{-1}.

Acknowledgments

The authors would like to thank the National Research Foundation of South Africa for funding under research grant number CSRP2204214088.

Authors contributions
The authors did all simulations and compiled the manuscript.

Availability of data and materials
All data presented in this article are available on request.

Conflict of interests
The authors declare that they have no known competing financial interests or personal relationships that could have appeared to influence the work reported in this paper.

References

[1] R. C. Klein and C. Weilandics. "Potential health hazards from lead shielding.". *Am. Ind. Hyg. Assoc J.*, **57**:1124–6, 1996. DOI: https://doi.org/10.1080/15428119691014215.

[2] M. I. Sayyed, K. M. Kaky, and R. A. Anaee. "Chromium ions effects on Sb_2O_3-PbO-GeO_2 glass properties for radiation protection.". *J. Theor. Appl. Phys.*, **17**:172355, 2023. DOI: https://doi.org/10.57647/j.jtap.2023.1705.55.

[3] G. J. Scuderi, G. V. Brusovanik, D. R. Campbell, R. P. Henry, B. Kwon, and A. R. Vaccaro. "Evaluation of non–lead-based protective radiological material in spinal surgery.". *Spine J.*, **6**:577, 2006. DOI: https://doi.org/10.1016/j.spinee.2005.09.010.

[4] M. I. Sayyed, H. O. Tekin, O. Kılıcoglu, O. Agar, and M. H. M. Zaid. "Shielding features of concrete types containing sepiolite mineral: comprehensive study on experimental, XCOM and MCNPX results. ". *Results Phys.*, **11**:40, 2018. DOI: https://doi.org/10.1016/j.rinp.2018.08.029.

[5] I. Akkurt, H. Akyildirim, B. Mavi, S. Kilincarslan, and C. Basyigit. "Gamma-ray shielding properties of concrete including barite at different energies. ". *Prog. Nucl. Energy*, **52**:620, 2010. DOI: https://doi.org/10.1016/j.pnucene.2010.04.006.

[6] H. O. Tekin, G. ALMisned, H. M. H. Zakaly, A. Zamil, D. Khoucheich, G. Bilal, G. L. Al-Sammarraie, S. A. M. Issa, M. S. Al-Buriahi, and A. Ene. "Gamma, neutron, and heavy charged ion shielding properties of Er^{3+}-doped and Sm^{3+}-doped zinc borate glasses. ". *Open Chem.*, **20**:130–45, 202. DOI: https://doi.org/10.1515/chem-2022-0128.

[7] E. S. A. Waly, M. A. Fusco, and M. A. Bourham. "Gamma-ray mass attenuation coefficient and half value layer factor of some oxide glass shielding materials. ". *Ann. Nucl. Energy*, **96**:26–30, 2016. DOI: https://doi.org/10.1016/j.anucene.2016.05.028.

[8] G. ALMisned, W. Elshami, S. Issa, G. Susoy, H. Zakaly, M. Algethami, Y. S. Rammah, A. Ene, S. A. Al-Ghamdi, A. A. Ibraheem, and H. O. Tekin. "Enhancement of Gamma-ray shielding properties in cobalt-doped heavy metal borate glasses: the role of lanthanum oxide reinforcement.". *Materials*, **14**:7703, 2021. DOI: https://doi.org/10.3390/ma14247703.

[9] S. Kaur and K. Singh. "Investigation of lead borate glasses doped with aluminium oxide as gamma ray shielding materials. ". *Ann. Nucl. Energy*, **63**:350–4, 2014. DOI: https://doi.org/10.1016/j.anucene.2013.08.012.

[10] I. Akkurt, R. Malidarre, and T. Kavas. "Monte Carlo simulation of radiation shielding properties of the glass system containing Bi_2O_3. ". *Eur. Phys. J. Plus*, **136**:264, 2021. DOI: https://doi.org/10.1140/epjp/s13360-021-01260-y.

[11] M. I. Sayyed, B. Elbashir, H. Tekin, E. Altunsoy, and D. Gaikwad. "Radiation shielding properties of pentaternary borate glasses using MCNPX code. ". *J Phys. Chem. Solids*, **121**:17–21, 2018. DOI: https://doi.org/10.1016/j.jpcs.2018.05.009.

[12] P. Sopapan, J. Laopaiboon, O. Jaiboon, C. Yenchai, and R. Laopaiboon. "Feasibility study of recycled CRT glass on elastic and radiation shielding properties used as X-ray and gamma-ray shielding materials.". *Prog. Nucl. Energy*, **119**:103149, 2020. DOI: https://doi.org/10.1016/j.pnucene.2019.103149.

[13] M. Sayyed, E. M. Çelikbilek, A. E. Ersundu, G. Lakshminarayana, and P. Kostka. "Investigation of radiation shielding properties for $MeOPbCl_2$ – TeO_2 (MeO = Bi_2O_3, MoO_3, Sb_2O_3, WO_3, ZnO) glasses. ". *Radiat. Phys. Chem.*, **144**:419–25, 2018. DOI: https://doi.org/10.1016/j.radphyschem.2017.10.005.

[14] J. Kaewkhao, A. Pokaipisit, and P. Limsuwan. "Study on borate glass system containing with Bi_2O_3 and BaO for gamma-rays shielding materials: Comparison with PbO.". *J. Nucl. Mater.*, **399**:38–40, 2010. DOI: https://doi.org/10.1016/j.jnucmat.2009.12.020.

[15] N. Chanthima, J. Kaewkhao, P. Limkitjaroenporn, S. Tuscharoen, S. Kothan, M. Tungjai, S. Kaewjaeng, S. Sarachai, and P. Limsuwan. "Development of BaO – ZnO – B_2O_3 glasses as a radiation shielding material.". *Radiat Phys Chem.*, **137**:72–7, 2017. DOI: https://doi.org/10.1016/j.radphyschem.2016.03.015.

[16] B. V. Kheswa. "X-ray shielding properties of bismuth-borate glass doped with rare-earth ions. ". *Open Chem.*, **21**:20220345, 2023. DOI: https://doi.org/10.1515/chem-2022-0345.

[17] Y. Al-Hadeethi, M. I. Sayyed, H. Mohammed, and L. Rimondini. "X-ray photons attenuation characteristics for two tellurite based glass systems at dental diagnostic energies. ". *Ceram Int.*, **46**:251–257, 2020. DOI: https://doi.org/10.1016/j.ceramint.2019.08.258.

[18] M. H. A. Mhareb. "Physical, optical and shielding features of Li_2O – B_2O_3 – MgO – Er_2O_3 glasses co-doped of Sm_2O_3. ". *Appl. Phys. A*, **126**:71, 2020. DOI: https://doi.org/10.1007/s00339-019-3262-9.

[19] S. Kaewjaeng, S. Kothan, W. Chaiphaksa, N. Chanthima, R. Rajaramakrishna, H. J. Kim, and J. Kaewkhao. "High transparency La_2O_3-$CaOB_2O_3$-SiO_2 glass for diagnosis X-rays shielding material application.". *Radiat. Phys. Chem.*, **160**:41–47, 2019. DOI: https://doi.org/10.1016/j.radphyschem.2019.03.018.

[20] B. Aktas, S. Yalcin, K. Dogru, Z. Uzunoglu, and D. Yilmaz. "Structural and radiation shielding properties of chromium oxide doped borosilicate glass.". *Radiat. Phys. Chem.*, **156**:144–149, 2019. DOI: https://doi.org/10.1016/j.radphyschem.2018.11.012.

[21] B. Aktas, A. Acikgoz, D. Yilmaz, S. Yalcin, K. Dogru, and N. Yorulmaz. "The role of TeO_2 insertion on the radiation shielding, structural and physical properties of borosilicate glasses. ". *J. Nucl. Mater.*, **563**:153619, 2022. DOI: https://doi.org/10.1016/j.jnucmat.2022.153619.

[22] M. Fidan, A. Acikgoz, G. Demircan, D. Yilmaz, and B. Aktas. "Optical, structural, physical, and nuclear shielding properties, and albedo parameters of TeO_2–BaO–B_2O_3–PbO–V_2O_5 glasses.". *J. Phys. Chem. Solids*, **163**:110543, 2022. DOI: https://doi.org/10.1016/j.jpcs.2021.110543.

[23] B. B. Solak, B. Aktas, D. Yilmaz, S. Kalecik, S. Yalcin, A. Acikgoz, and G. Demircan. "Exploring the radiation shielding properties of B_2O_3-PbO-TeO_2-CeO_2-WO_3 glasses: A comprehensive study on structural, mechanical, gamma, and neutron attenuation characteristics.". *Mater. Chem. Phys.*, **312**:128672, 2024. DOI: https://doi.org/10.1016/j.matchemphys.2023.128672.

[24] N. Yorulmaz, M. M. Yasar, A. Acikgoz, Y. Kavun, G. Demircan, M. Kamislioglu, B. Aktas, and E. O. Ulas. "Influence of Gd_2O_3 on structural, optical, radiation shielding, and mechanical properties of borate glasses. ". *Opt. Mater.*, **149**:115032, 2024. DOI: https://doi.org/10.1016/j.optmat.2024.115032.

[25] M. Fidan, A. Acikgoz, D. Yılmaz, G. Demircan, S. Kalecik, B. Aktas, and S. Isgor. "Investigation of the structural, mechanical, radiation and neutron shielding properties of the TeO_2-B_2O_3-Li_2O-MoO_3-CuO glass system.". *J. Alloys Compd.*, **976**:172981, 2024. DOI: https://doi.org/10.1016/j.jallcom.2023.172981.

[26] H. A. Saudi, H. M. H. Zakaly, S. A. M. Issa, H. O. Tekin, M. M. Hessien, Y. S. Rammah, and A. M. A. Henaish. "Fabrication, FTIR, physical characteristics and photon shielding efficacy of CeO_2/sand reinforced borate glasses: Experimental and simulation studies. ". *Radiat. Phys. Chem.*, **191**:109837, 2022. DOI: https://doi.org/10.1016/j.radphyschem.2021.109837.

[27] B. Subedi and T. R. Lamichhane. "Radiation shielding properties of low-density Ti-based bulk metallic glass composites: a computational study. ". *Phys. Scr.*, **98**:035003, 2023. DOI: https://doi.org/10.1088/1402-4896/acb623.

[28] N. Tuncel, I. Akkurt, I. Atik, R. B. Malidarre, and M. I. Sayyed. "Neutron-gamma shielding properties of chalcogenide glasses.". *Radiat. Phys. Chem.*, **218**:111582, 2024. DOI: https://doi.org/10.1016/j.radphyschem.2024.111582.

[29] B. Aygün, N. Yıldız Yorgun, M. I. Sayyed, and A. Karabulut. "$Li_2B_4O_7$–Bi_2O_3–ZrO_4–$CaWO_4$ glass system for neutron protection in neutron applications. ". *Prog. Nucl. Energy*, **162**:104751, 2023. DOI: https://doi.org/10.1016/j.pnucene.2023.104751.

[30] M. Aygun. "Gamma-ray, fast neutron and charged particle shielding performance of $15Li_2O$-$25BaO$-$(40-x)B_2O_3$-$20P_2O_5$-xDy_2O_3 glass system. ". *Radiat. Phys. Chem.*, **219**:111671, 2024. DOI: https://doi.org/10.1016/j.radphyschem.2024.111671.

[31] S. Alomairy, M. S. Al-Buriahi, E. A. Abdel Wahab, C. Sriwunkum, and Kh. S. Shaaban. "Synthesis, FTIR, and neutron/charged particle transmission properties of Pb_3O_4–SiO_2–ZnO–WO_3 glass system.". *Ceram. Int.*, **47**:17322–17330, 2021. DOI: https://doi.org/10.1016/j.ceramint.2021.03.045.

[32] " ". .

[33] A. M. Babeer, H. Y. Amin, M. I. Sayyed, A. E. Mahmoud, M. A. Abdo, T. E. Ellakwa, and M. S. Sadeq. "Impact of mixed heavy metal cations (Ba and Bi) on the structure, optical and ionizing radiation shielding parameters of Bi_2O_3–BaO–Fe_2O_3–SrO–B_2O_3 glass matrix.". *Ceram. Int.*, **50**:19245–19258, 2024. DOI: https://doi.org/10.1016/j.ceramint.2024.03.024.

[34] " ". .

[35] E. Sakar, O. Ozpolat, B. Alım, M. Sayyed, and M. Kurudirek. "Phy-X/PSD: Development of a user friendly online software for calculation of parameters relevant to radiation shielding and dosimetry. ". *Radiat. Phys. Chem.*, **166**:108496, 2020. DOI: https://doi.org/10.1016/j.radphyschem.2019.108496.

[36] I. Akkurt. "Effective atomic and electron numbers of some steels at different energies. ". *Ann. Nucl. Energy*, **26**:1702–1705, 2009. DOI: https://doi.org/10.1016/j.anucene.2009.09.005.

[37] B. V. Kheswa and S. N. T. Majola. "Impact of Bi_2O_3 on the X-ray shielding characteristics of telluro-borate-bismuth glass for medical applications.". *J. Theor. Appl. Phys.*, **18**:182438, 2024. DOI: https://doi.org/10.57647/j.jtap.2024.1803.38.

[38] H. A. Thabit, A. K. Ismail, A. Saeed, D. A. Abdulmalik, A. Bafaqeer, H. S. Naeem, and M. I. Sayyed. "Enhancing gamma-ray shielding with Bi_2O_3-Enriched BTBi glasses: Optimal balance of attenuation and glass transparency. ". *Ceram. Int.*, , 2024. DOI: https://doi.org/10.1016/j.ceramint.2024.05.176.

[39] S. Biradar, A. Dinkar, Manjunatha, A. S. Bennal, G. B. Devidas, B. T. Hareesh, M. K. Siri, K. N. Nandan, M. I. Sayyed, H. Es-soufi, and M. N. Chandrashekara. "Comprehensive investigation of borate-based glasses doped with BaO: An assessment of physical, structural, thermal, optical, and radiation shielding properties. ". *Opt. Mater.*, **150**:115176, 2024. DOI: https://doi.org/10.1016/j.optmat.2024.115176.